Unraveling the Reasons for Efficiency Loss in Perovskite Solar Cells

Yong Hui Lee, Jingshan Luo, Robin Humphry-Baker, Peng Gao, Michael Grätzel, and Mohammad Khaja Nazeeruddin**

The effect of the presence of unreacted PbI_2 on the perovskite solar cells efficiency is reported. *N*,*N*-Dimethylformamide vapor treatment is introduced to study the influence of complete conversion to a power conversion efficiency of the device. It is discovered that the optimized morphology of the PbI_2 under layer is essential to form a dense perovskite layer preventing recombination by direct contact between TiO_2 and a hole transporting layer, and to increase the charge collection efficiency. The present findings provide an insight into the morphology and growth mechanism of perovskite layer, the correlation between the device performance, and the film deposition process.

1. Introduction

Efficient energy conversion between electrons and photons is one of the central challenges facing the world today and solar photovoltaics (PV) represent the ultimate goal in the quest for clean, renewable electricity generation. For decades, many researchers have attempted to develop solar cells with high efficiency and low cost that are based on dye-sensitized,[1] and polycrystalline thin-film semiconductors. Recent reports on organic–inorganic perovskite-based semiconductors, pioneered by Mitzi et al., reveal their remarkable potential for producing high-efficiency low-cost thin-film solar cells.[2–6] The methyl ammonium/formamidinium lead halide perovskite solar cell is of primary interest due to its superior performance compared to dye-sensitized solar cells and has achieved a power conversion efficiency (PCE) over 20%.[7] Various perovskite materials such as $MAPbX_3$ (X = Cl, Br, I), and deposition methods have been investigated to further improve the PCE of perovskite solar cells.[8–19] The solution method normally can be described as an one-step[3] or a two-step[16] method according to the details in the preparation procedures. There has been a rapid development and understanding in both methods. With the one-step method, Snaith and co-workers firstly showed the importance of the coverage with perovskite layers to get high open-circuit voltage (V_{oc}).[17,20,21] Recently, Seok and co-workers achieved the 17.9% PCE with additional solvent engineering.[22] These studies suggest that an optimum structural design of the perovskite layers is the key factor to get high efficiency. The two-step method is another way for reproducible deposition of perovskite layers. It is known that this technique enables an excellent coverage of perovskite absorbers on the mesoporous-TiO_2 (mp-TiO_2) surface, which leads to a high PCE. For example, the deposition of $MAPbI_3$ is done by the sequential method, firstly by depositing PbI_2 layer, followed by conversion to perovskite by reacting with CH_3NH_3I (MAI). Thus, the successful conversion of PbI_2 to perovskite is necessary to guarantee enough light harvesting.[15,23,24] However, evidence for residual PbI_2 is still found even in many of the high efficiency devices.[14,16,23] The enhancement of product lifetime and device performance with PbI_2-rich films are observed regardless of the deposition method,[25–27] which implies that the coexistence of PbI_2 can be beneficial for the device performance. To our knowledge, no in-depth study on the presence of unreacted PbI_2 with the two-step solution method has been reported so far. Therefore, we believe that an understanding of the exact phenomenon happening during the conversion of PbI_2 to perovskite and the influence of these results on device performance is quite important.

In this work, we studied the influence of the unreacted PbI_2 on the device performance, particularly on the structural aspects. The morphological changes during the conversion, the role of PbI_2 in the formation of the perovskite film and influence of the presence of unreacted PbI_2 on device performance are discussed. Finally, we suggest an efficient architecture for the high efficiency perovskite solar cells with our novel findings.

Dr. Y. H. Lee, Dr. P. Gao, Prof. M. K. Nazeeruddin
Group for Molecular Engineering of Functional Materials
Institute of Chemical Sciences and Engineering
École Polytechnique Fédérale de Lausanne
CH-1015 Lausanne, Switzerland
E-mail: yonghui.lee@epfl.ch; mdkhaja.nazeeruddin@epfl.ch

Dr. J. Luo, Dr. R. Humphry-Baker, Prof. M. Grätzel
Laboratory of Photonics and Interfaces
Institute of Chemical Sciences and Engineering
École Polytechnique Fédérale de Lausanne
CH-1015 Lausanne, Switzerland

Prof. M. K. Nazeeruddin
Center of Excellence for Advanced Materials Research (CEAMR)
King Abdulaziz University
Jeddah 21589, Saudi Arabia

DOI: 10.1002/adfm.201501024

2. Results and Discussion

2.1. Layer Morphology in the Conversion of PbI_2 to Perovskite

As mentioned in the introduction, we find PbI_2 on the perovskite films regardless of efficiency of the devices when the two-step method is used. Assuming that the main factor to determine the device performance is the presence of PbI_2, we can think of two different solutions. The first would be complete conversion of PbI_2 to perovskite. The other should be making best use of unreacted PbI_2. Considering that the two-step solution dipping method is used for perovskite preparation, an extension of reaction time such as longer dipping of PbI_2 films in MAI solution or postheating of the perovskite film can be tested to further improve the conversion. However, it is known that there is a limit in conversion due to a short diffusion length between PbI_2 and MAI.[16] And, loss of MAI may occur during the excessive thermal heating. To resolve these issues, a post-*N*,*N*-dimethylformamide (DMF) vapor treatment was applied. We expected that the DMF vapor would dissolve the PbI_2/perovskite layer, and promote the further mixing. For the treatment, a prepared perovskite film (labeled as Film A) was kept in a glass petri dish, containing 100 µL of DMF on the bottom of the dish. The film was left in enclosed DMF atmosphere for 1 min, and began to change its color from dark brown to yellow and finally to yellowish white. The original dark brown color was recovered when it was heated at 70 °C for 10 min (Film B). Morphological changes at the sequential steps are observed with scanning electron microscopy (SEM) analysis. **Figure 1**a,d shows top-view and cross-sectional images of the as-prepared perovskite film on the FTO/bl-TiO_2/mp-TiO_2 (hereafter TiO_2 substrate). The film looks dense with fully covered perovskite layer over the TiO_2 substrate but not flat due to the existence of irregular cuboid particles. After exposure to DMF vapor, the morphology of the film changes dramatically. The film was dried at 70 °C for 10 min before the analysis. The SEM image of this film displays porous and overall smooth morphology made of aggregated spherical particles over the film (Figure 1b,e). Perovskite cuboids shown in the Film A are not found in the Film B. Furthermore, we found out that this morphology transformation was reversible. After dipping the film B in a MAI solution again for 30 s, the film was completely covered with cubic particles again (Film C, Figure 1c,f), but exhibiting much larger grain size compared with Film A. We believe this comes from the blocking effect of the earlier perovskite layer on further MAI reaction in the solution method. It appears that the growth mechanism of the perovskite crystal in the solution dipping method is closer to dissolution and recrystallization at the solid–liquid interface, usually near the surface of PbI_2, rather than the interlayer diffusion shown in the one-step method. In this case, fast nucleation and growth can form a dense perovskite layer over the PbI_2 surface which hinders the further supply of precursors. Thus, we cannot observe noticeable improvement in conversion though we dip the as-prepared perovskite film twice or for longer time in the MAI solution. In this respect, the morphology of the Film C is quite interesting but contrasting to our previous understanding. The perovskite layer was combined of isolated particles rather than a continuous layer, which resulted in exposure of the TiO_2 layer as shown in Figure 1c.

2.2. Photophysical Characteristics

According to the X-ray diffraction (XRD) analysis, the perovskite Film A (Figure 2a) exhibits a strong peak of PbI_2 at 12.58° caused by a stoichiometric imbalance between PbI_2 and MAI of the initial film. And the peak of PbI_2 is still found even after DMF vapor treatment (Film B). However, complete conversion was observed when the Film B was dipped again in the MAI solution. The peak of PbI_2 has disappeared from the film and the intensity of the perovskite peaks have increased further compared to both Film A and Film B. We found the film swiftly turns black during the dipping, which indicates a morphological change has enhanced the optical absorption of the film as shown in **Figure 2**b. In hypothesis, the growth of the perovskite particle shown in Film C was derived from the further consumption of PbI_2 underneath and inside of the perovskite layer. And we attribute the complete conversion to the presence of microchannels generated by the DMF treatment or a catalytic effect of the as-prepared perovskite particles mixed beforehand. These findings clearly demonstrate the presence of PbI_2 in the perovskite with a normal two-step method, particularly with DMF-based PbI_2 precursors. The results also show the difficulty in making a compact layer without assistance of the PbI_2 layer. On the other hand, the comparison of *J*–*V* curves of the complete cells (Cell A and Cell C) assembled with spiro-OMeTAD and Au counter electrode displays diametrically opposite results. A severe drop of the PCE was observed from the Cell C (fabricated with Film C) due to decreased V_{oc} and short-circuit current density (J_{sc}) despite slightly improved fill factor (FF). A decrease of more than 150 mV of V_{oc} and 6 mA of J_{sc} was measured

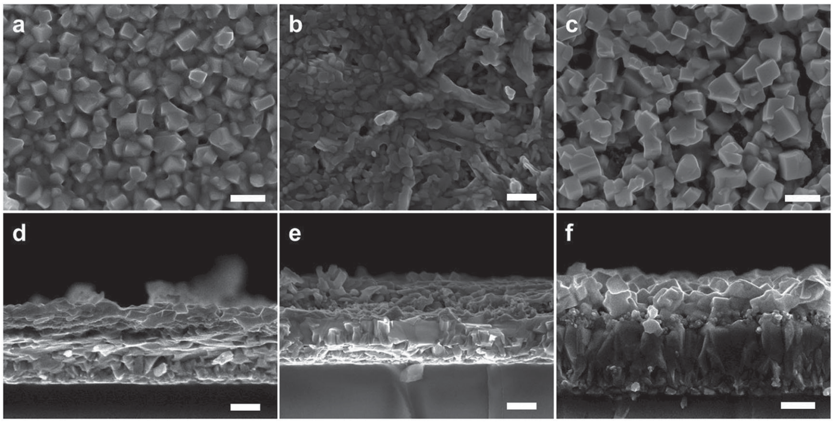

Figure 1. SEM top-view (top) and cross-sectional (bottom) images. a,d) As-prepared perovskite film (Film A). b,e) After exposure to DMF vapor and drying at 70 ° for 10 min (Film B). c,f) After second dipping in MAI solution and drying at 70°C for 10 min (Film C). Scale bar, 300 nm.

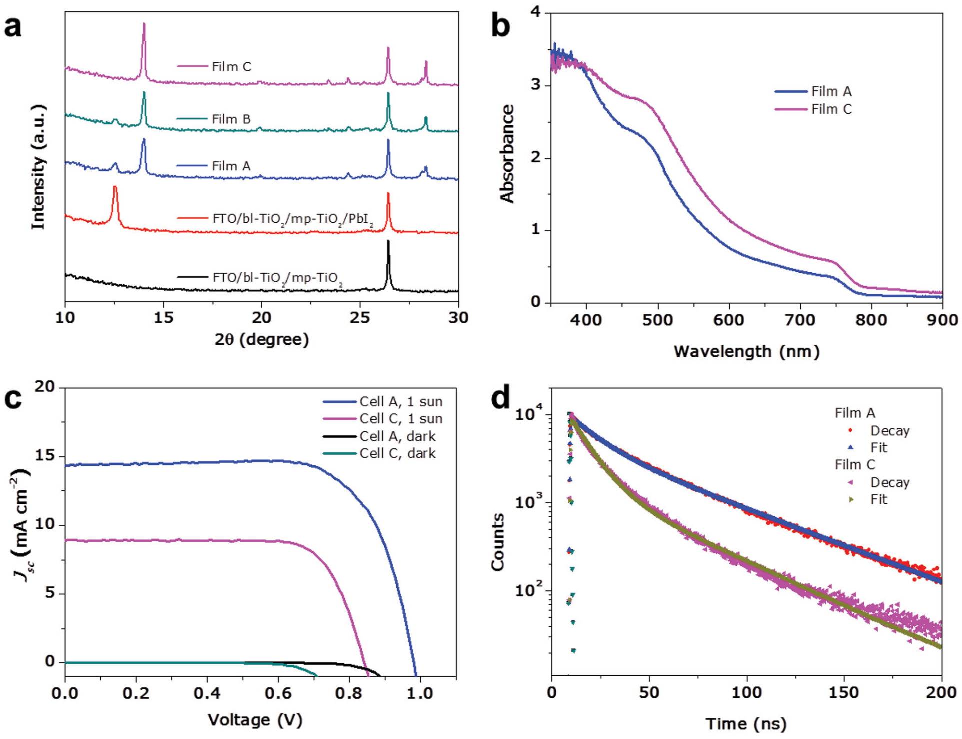

Figure 2. Photophysical properties of the films and the devices before and after DMF treatment. a) X-ray diffraction patterns of the films. The black line is obtained from the FTO/bl-TiO_2/mp-TiO_2 substrate. The red line is from the FTO/bl-TiO_2/mp-TiO_2/PbI_2 film. Film A, B, C represents XRD patterns of the perovskite films obtained from the as-prepared, after the exposure to DMF and after second dipping in MAI solution, respectively. b) Absorbance spectra of Film A and Film C. c) *J*–*V* curves of the complete cells. Cell A and Cell C were made using Film A and Film C, and spiro-OMeTAD and Au electrode, respectively. d) Photoluminescence (PL) decay curves of Film A and Film C.

compared to the Cell A as shown in Figure 2c. And, the photoluminescence (PL) decay curves demonstrated in Figure 2d and Table S1 (Supporting Information) also supported the trend shown in the *J*–*V* curves. The longer lifetime was observed in the as-deposited film (Film A), indicating less recombination in the original film. Cross-sectional SEM images (Figure S1, Supporting Information) display that the drop in the PCE might be predominantly due to the recombination between TiO_2 and hole transporting material (HTM) rather than between perovskite and gold electrode. These results indicate the existence of PbI_2 could be helpful for the device performance. A successive color change of the real films are visually shown in Figure S2 (Supporting Information).

Figure 3 depicts a schematic of the interface between PbI_2/perovskite and pure perovskite layers. Perovskite layers are formed densely by the assistance of PbI_2 under layers and connected to TiO_2 layers through the partially open pores above the PbI_2 layer. In this case, PbI_2 layer is beneficial for the cell, and consequently has a natural cascade structure as depicted in the energy band gap diagram. The other benefit of this is intimacy of TiO_2 and perovskite interfaces assisted by PbI_2 interlayer, which may be the reason of longer lifetime shown in the PL decay. On the other hand, cells can undergo severe recombination when the perovskite layer is not dense. If the spiro-OMeTAD can contact directly the TiO_2 surface, it will generate a loss channel for charge collection as discussed in other reports.[17,20,21] We believe this explains why there was such a high drop of the PCE in the Cell C (Figure 1c).

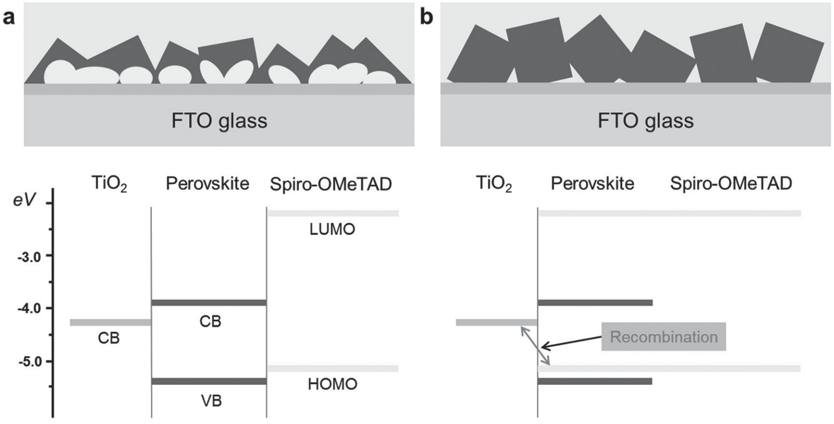

Figure 3. An illustration showing a structural difference between a) as-prepared and b) DMF-treated films. The bright spherical layer and dark cubic crystals represent PbI_2 and perovskite layers, respectively. Spiro-OMeTAD is shown as a capping layer. Consequential energy band gap diagrams are compared below each structure.

The above insight has motivated us to explore further to an efficient morphology for the PbI_2 and perovskite films. In our

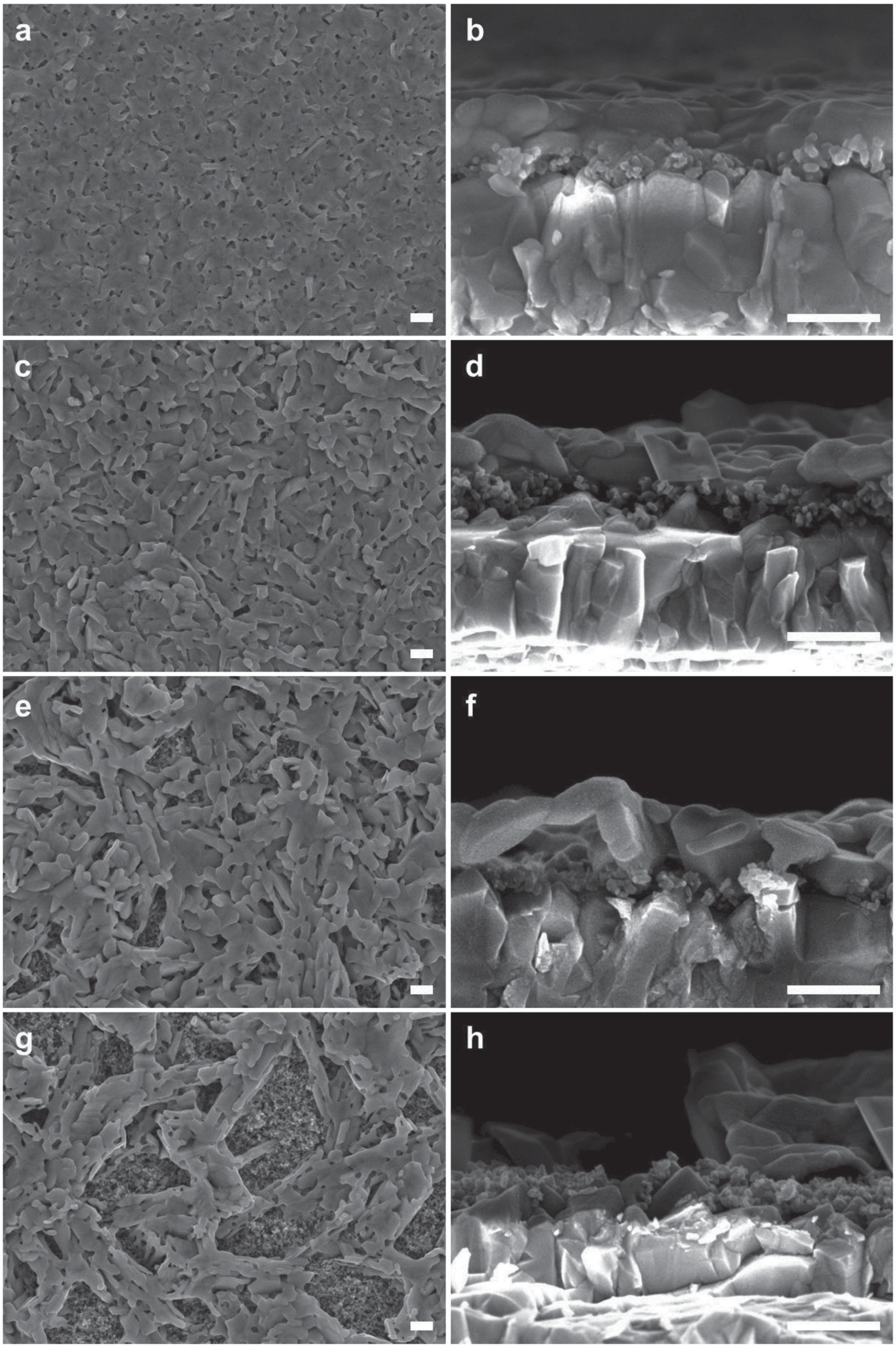

Figure 4. SEM top-view and cross-sectional images of PbI_2-coated films. Films (a,b), (c,d), (e,f), and (g,h) are prepared using TiO_2 substrates released in air for 1, 3, 5, and 7 min, respectively. Scale bar, 300 nm.

experiments using the two-step solution method, we easily find that the final morphology of the PbI_2 layer can be influenced by many factors such as the difference of the thickness, pore size, and surface roughness of the substrate. Furthermore, the concentration of the PbI_2 and MAI precursor solutions, speed and duration time during the spin-coating, heating temperature and humidity also affect the results. All these factors are strongly related to the final PCE. The PbI_2 films were prepared outside a drybox while the sequential steps were done inside the drybox. With the other conditions unchanged, the films

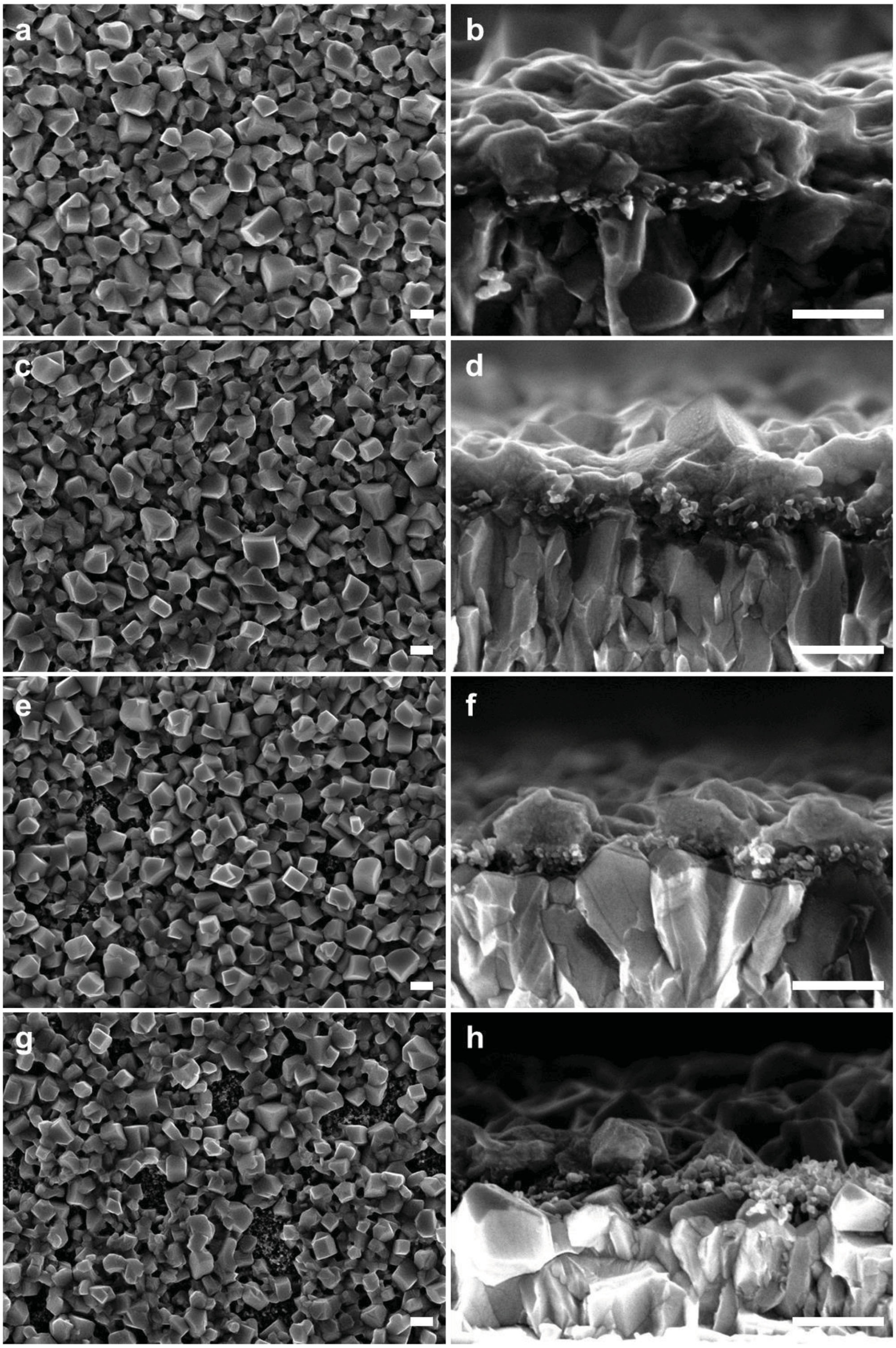

Figure 5. SEM top-view and cross-sectional images of perovskite-coated films. Film (a,b) is made from film (a,b) of Figure 4. Likewise, films (c,d), (e,f), and (g,h) are made from films (c,d), (e,f), and (g,h) of Figure 4. Scale bar, 300 nm.

would be affected dominantly by humidity. **Figure 4** shows the morphological change of PbI_2 layers as a function of exposure time in air of TiO_2 substrates. First, all the TiO_2 substrates were sintered at 500 °C for 30 min, cooled down to 100 °C, and then kept at 100 °C for 10 min. Finally, they were placed on a glass plate at room temperature before coating of PbI_2. The PbI_2 film showed thicker and less porous morphology when the PbI_2 precursor was coated after cooling the TiO_2 substrate for 1 min (Figure 4a,b). At longer time, the films became more porous with decreased TiO_2 surface coverage by the influence of

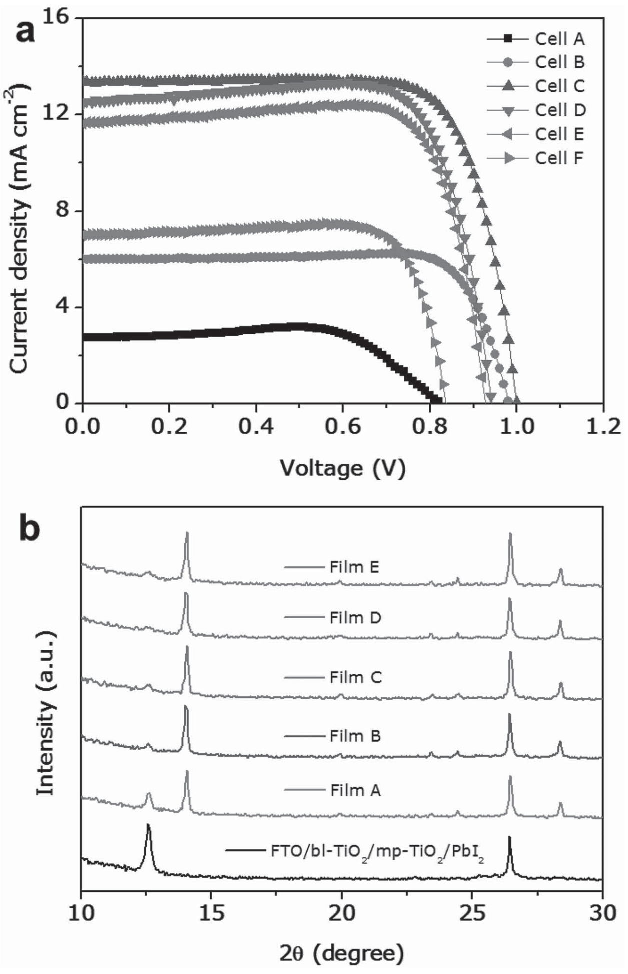

Figure 6. *J–V* curves of the devices and XRD patterns using the controlled perovskite films. a) Before the coating of PbI$_2$, TiO$_2$ substrates were released in air for 30 s (Cell A), 1 min (Cell B), 3 min (Cell C), 5 min (Cell D), 7 min (Cell E), and 15 min (Cell F), respectively. b) Film A is made of the TiO$_2$ substrate released in air for 1 min. Film B to Film E corresponds 3, 5, 7, and 15 min, respectively. The XRD pattern of PbI$_2$ reference film was also measured and demonstrated for the comparison.

moisture as shown in the top-view images and cross-sectional images (Figure 4c–h). Those PbI$_2$ films were converted to perovskite films by reacting with MAI solution. There was no big difference in the size of perovskite crystals (**Figure 5**). However, with respect to the surface coverage, it looks lower than that of the PbI$_2$-coated films but it also begins to show TiO$_2$ surface from the samples released for 5 min (Figure 5e,f), and the exposure of TiO$_2$ surface became prominent after 7 min (Figure 5g,h). The gradual decrease in thickness of the perovskite layer was also observed over the films.

We fabricated perovskite solar cells with the above films, and found a very interesting result from the *J–V* measurement (**Figure 6**). The best PCE was obtained from the perovskite film made of the TiO$_2$ substrate which was exposed for 3 min in air. V_{oc} and FF reached values of 1.0 V and 76%, respectively, though J_{sc} showed a lower value of 13.4 mA cm^{-2}; while other cells showed not only lower efficiencies but also displayed curves that were distorted from normal behavior. For the lowest PCE cell, V_{oc} started at 0.82 V and gradually increased until the highest value of 1.0 V in the best devices. Then, it gradually decreased again to 0.83 V. A similar trend was also shown in the J_{sc} values. Based on our previous findings from the SEM analysis, we attribute these changes to the morphological change of PbI$_2$ underlayers. The existence of PbI$_2$ in all films is demonstrated by XRD analysis (Figure 6b). As expected, PbI$_2$ peaks are detected in every film as discussed in Figure 2. However, it is noteworthy that the device performance can be changed extremely by the morphological change of the PbI$_2$ underlayer. It is thought that a thicker and denser PbI$_2$ layer limits the infiltration of MAI solution, hindering conversion of PbI$_2$ to perovskite. The cell fabricated with the TiO$_2$ substrate which was exposed in air for 30 s exhibited a highly distorted *J–V* curve. It became less but it still showed an overshoot in the cell fabricated with the TiO$_2$ substrate exposed for 1 min. On the contrary, the film seems to face another problem when the PbI$_2$ film is too thin and not dense. The exposure of TiO$_2$ layer under the perovskite layer would happen when the perovskite film was prepared with TiO$_2$ substrates exposed in air for more than 5 min. Therefore, decrease of the PCE can be explained as the direct contact between TiO$_2$ and spiro-OMeTAD.

Figure 7 presents an illustration on the correlation between the morphology and the energy band gap diagram of the PbI$_2$/perovskite film. Three possible paths are depicted based on our observations. In path 1, PbI$_2$ will block the electron injection from perovskite to TiO$_2$, as the conduction band of PbI$_2$ is located higher than that of the perovskite.[28] A large accumulation of electrons may recombine with the holes. In path 3, electrons and holes can be transferred to the conduction band of TiO$_2$ and HOMO of spiro-OMeTAD, respectively, without any barrier. However, they can recombine easily before collection due to the direct contact between TiO$_2$ and spiro-OMeTAD. From the perspective of the recombination, by excluding path 1 and path 3, path 2 is the optimum path leads to the high efficiency.

To see the influence of the mp-TiO$_2$ layer, perovskite cells were made using the optimized conditions but the thickness of the mp-TiO$_2$ layer was varied as shown in **Table 1**. A gradual increase in J_{sc} is shown as the thickness of mp-TiO$_2$ increased and it reached the highest value of 19.04 mA cm^{-2} when the thickness is ca. 180 nm. It seems J_{sc} is not seriously

Table 1. Summarized PCEs as a function of the thickness of the mp-TiO$_2$ layer.

Cell name	Thickness of mp-TiO$_2$ layer [nm]	J_{sc} [mA cm^{-2}]	V_{oc} [V]	FF	PCE [%]
Cell 1	No mp-TiO$_2$ (flat)	3.01	0.91	0.72	2.05
Cell 2	100	13.36	1.00	0.76	10.30
Cell 3	150	17.87	1.03	0.72	13.60
Cell 4	180	19.04	1.02	0.75	14.56
Cell 5	200	18.20	1.03	0.72	13.63
Cell 6	220	17.84	1.01	0.72	13.00
Cell 7	260	18.93	0.97	0.68	12.66

dependent on the thickness of the mp-TiO_2 layer when it goes over 200 nm though small decrease is shown. Actually the use of the thick mp-TiO_2 layer is not recommended considering the risk of recombination by the contact with HTM and increase of series resistance which decreases FF. For V_{oc}, every cell using mp-TiO_2 layers showed similar value of around 1.0 V. We also fabricated a flat-type cell which has no mp-TiO_2 layer (cell 1), but it exhibited quite low values in J_{sc}, V_{oc}, FF, and the PCE, probably due to the deficient moisture absorption.

The current–voltage curve, incident photon to current conversion efficiency (IPCE), and photocurrent transient data of the cell with 180 nm thick mp-TiO_2 electrode (Cell 4 of Table 1) are shown in **Figure 8**. The *J–V* curve was smooth at the scanning setting time of 200 ms for 10 mV without a distinguished bump. The integrated current density from IPCE measurement was a slightly higher but acceptably matched with J_{sc} from the *J–V* curve. According to the photocurrent transient measurement, the cell showed sharp and linear photocurrent behavior with the time over all the light intensities

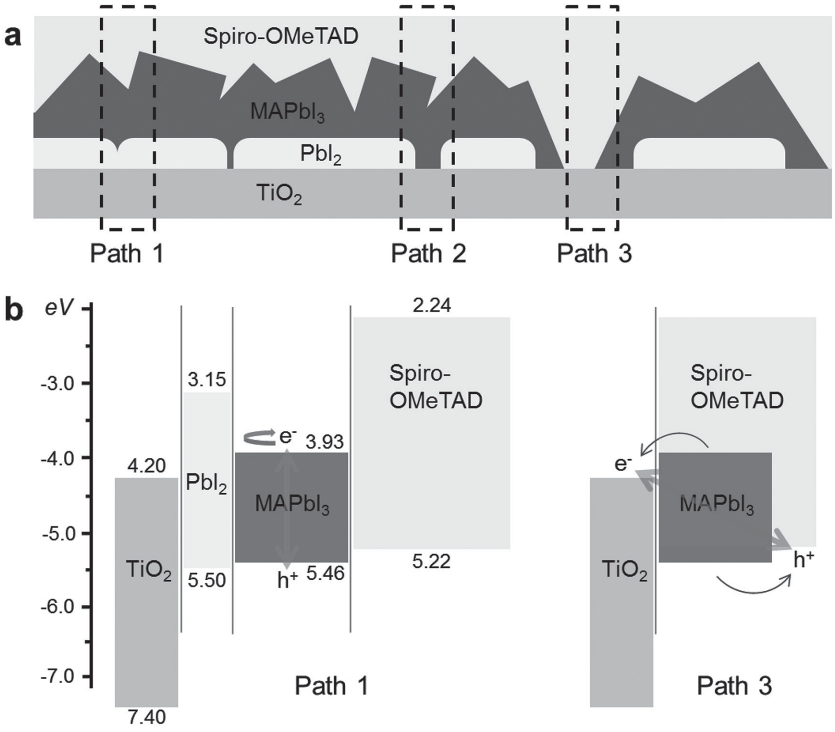

Figure 7. An illustration demonstrating recombination paths by the structure. a) Three possible paths on the perovskite film. b) Energy band gap diagrams for path 1 and path 3.

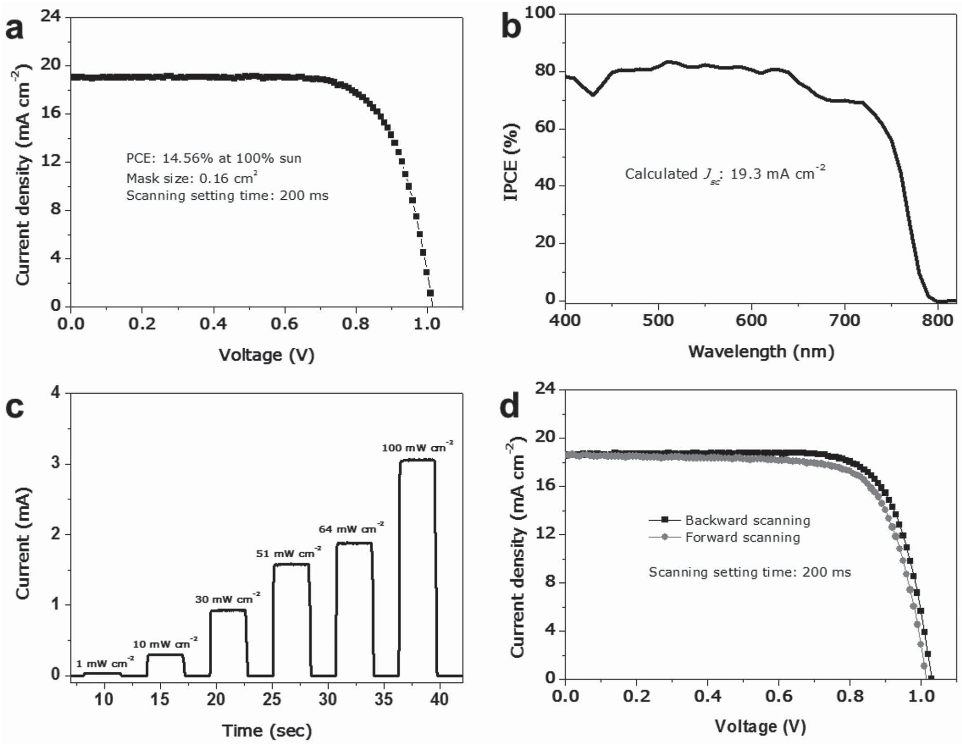

Figure 8. Electrical properties of the perovskite solar cell with 180 nm thick mp-TiO_2 electrode. a) *J–V* curve, b) IPCE, c) Photocurrent dynamics, and d) *J–V* curve hysteresis by scanning forward and backward.

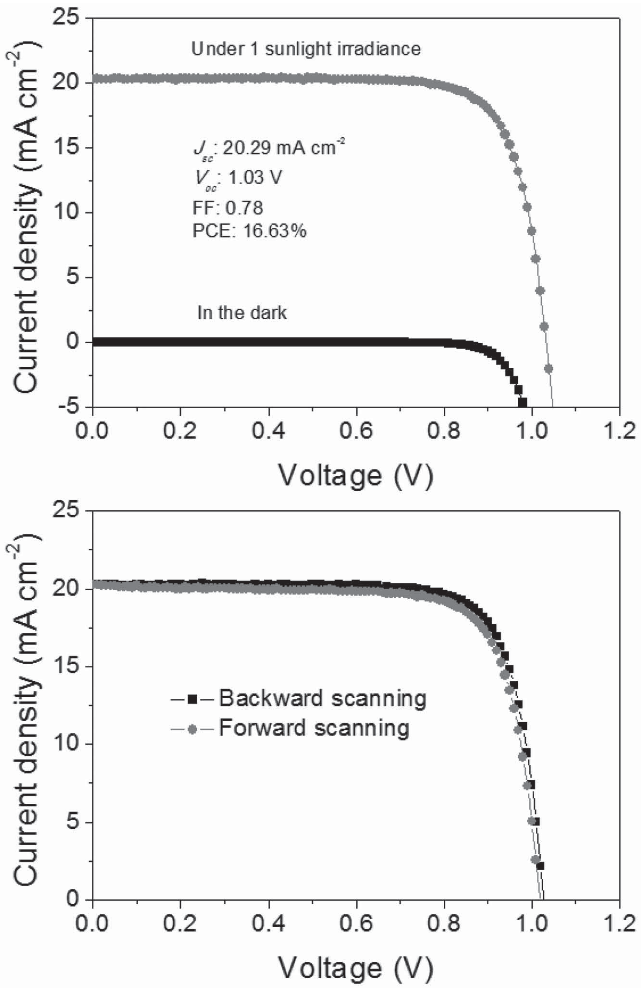

Figure 9. Current–voltage characteristics of the champion cell (top) and *J*–*V* curve hysteresis by scanning forward and backward (bottom).

indicating normal behavior of the device. We compared the *J*–*V* curves at different scanning directions. A small hysteresis was still observed as noted in some other reports.[19] Finally, the best PCE of 16.63% with small hysteresis was obtained from the optimized condition as shown in **Figure 9**.

3. Conclusion

We studied the efficiency of perovskite solar cells focusing on the morphological aspects. The complete conversion of PbI_2 to perovskite was successfully achieved by DMF vapor treatment. However, serious recombination was also observed due to the exposure of TiO_2 layer to the HTM. The importance of this work can be emphasized in two aspects. The first is that the high device performance can be achieved despite the presence of PbI_2. We also investigated that the device performance is highly influenced by the morphology of the PbI_2 layer, which determines the coverage of the perovskite layer. Our findings suggest that the higher PCE can be achieved by further control of the recombination paths associated with the morphology of the PbI_2 layer.

4. Experimental Section

Device Fabrication: Chemically etched FTO glass (Nippon Sheet Glass) was cleaned with detergent solution, acetone, and ethanol. To form a 20 nm thick TiO_2 blocking layer, diluted titanium diisopropoxide bis(acetylacetonate) (TAA) solution (Sigma-Aldrich) in ethanol was sprayed at 450 °C. Mesoporous-TiO_2 layers were made by spin-coating a commercially available TiO_2 paste (Dyesol 30NRD). Substrates were baked at 500 °C for 30 min before the deposition of the perovskite layer. The two-step method was used to make the perovskite film. First, 1.0 M of PbI_2 solution was prepared by mixing 461 mg of PbI_2 (Aldrich) in 1 mL of DMF. The solution was stirred at 70 °C for 30 min, and spin-coated at 6500 rpm for 20 s on TiO_2 substrates, and the film was dried at 70 °C for 15 min. The film was dipped in MAI solution (8 mg of MAI in 1 mL of IPA) for 20 s, rinsed with IPA and dried at 70 °C for 5 min. The spiro-OMeTAD was spin-coated at 3000 rpm for 20 s before deposition of the 60 nm thick Au electrode by a thermal evaporation. The HTM solution was made by dissolving 72.3 mg of spiro-OMeTAD, 28.8 μL of 4-*tert*-butylpyridine (TBP, Aldrich), 17.5 μL of a stock solution of 520 mg mL^{-1} of lithium bis(trifluoromethylsulphonyl)imide in acetonitrile and 29 μL of a stock solution of 300 mg mL^{-1} of tris(2-(1*H*-pyrazol-1-yl)-4-*tert*-butylpyridine)cobalt(III) bis(trifluoromethylsulphonyl)-imide in acetonitrile in 1 mL of chlorobenzene. All the preparative work to deposit PbI_2, perovskite, and spiro-OMeTAD were done inside the drybox to minimize the influence of moisture while the controlled PbI_2 films were prepared outside the drybox.

Film Characterization: XRD analysis was carried out using Bruker D8 Advance diffractometer in an angle range of $2\theta = 10°–30°$. All of SEM images were obtained using Zeiss Merlin. The absorbance was measured with 102 mm diametered integration sphere (Horiba F-3018). The measurements were conducted in a Fluorolog 322 (Horiba Jobin Yvon Ltd Spectrofluorometer). Samples were illuminated with by a 450 W Xe lamp filtered through a double monochromator (5 nm landpass) directed onto the sample. The photoluminescence dynamics were measured using the time-resolved single photon counting (TRSPC) technique that is incorporated into the same Fluorolog-312 spectrofluorometer. The exciting source is now a NANOLed 406 nm pulsed diode laser with a pulse width of less than 200 ps and repetition rate of 1 MHz. A 610 nm high pass filter was used to exclude stray photon reaching the detector that can result from scattering from the sample. The TRSPC data were reconvoluted with a simple two exponential model. This resulted in two characteristic lifetimes (1 and 2) for each sample. The relative amplitude of each component (A1, A2) was also noted.

Device Measurement: Current–voltage characteristics were recorded by applying an external potential bias to the cell while recording the generated photocurrent with a digital source meter (Keithley Model 2400). The light source was a 450 W xenon lamp (Oriel) equipped with a SchottK113 Tempax sunlight filter (Praezisions Glas & Optik GmbH) to match the emission spectrum of the lamp to the AM1.5G standard. Before each measurement, the exact light intensity was determined using a calibrated Si reference diode equipped with an infrared cutoff filter (KG-3, Schott). IPCE spectra were recorded as functions of wavelength under a constant white light bias of ≈10 mW cm^{-2} supplied by an array of white light emitting diodes. The excitation beam coming from a 300 W xenon lamp (ILC Technology) was focused through a Gemini-180 double monochromator (Jobin Yvon Ltd) and chopped at ≈2 Hz. The signal was recorded using a Model SR830 DSP Lock-In Amplifier (Stanford Research Systems). All measurements were conducted using a nonreflective metal aperture of 0.16 cm^2 to define the active area of the device and avoid light scattering through the sides.

Supporting Information

Supporting Information is available from the Wiley Online Library or from the author.

Acknowledgements

The authors acknowledge funding from the European Union Seventh Framework Programme [FP7/2007-2013] under Grant Agreement No. 604032 of the MESO project (FP7/2007-2013) ENERGY.2012.10.2.1; NANOMATCELL, Grant Agreement No. 308997. M.G. thanks the European Research Council (ERC) for financial support under the advanced research grant (ARG 247404) "Mesolight."

Received: March 15, 2015
Revised: April 18, 2015

---

[1] B. O'Regan, M. Grätzel, *Nature* **1991**, *353*, 737.

[2] D. B. Mitzi, C. A. Field, W. T. A. Harrison, A. M. Guloy, *Nature* **1994**, *369*, 467.

[3] A. Kojima, K. Teshima, Y. Shirai, T. Miyasaka, *J. Am. Chem. Soc.* **2009**, *131*, 6050.

[4] H.-S. Kim, C.-R. Lee, J.-H. Im, K.-B. Lee, T. Moehl, A. Marchioro, S.-J. Moon, R. Humphry-Baker, J.-H. Yum, J. E. Moser, M. Grätzel, N.-G. Park, *Sci. Rep.* **2012**, *2*, 591.

[5] L. Etgar, P. Gao, Z. Xue, P. Qin, A. K. Chandiran, B. Liu, M. K. Nazeeruddin, M. Grätzel, *J. Am. Chem. Soc.* **2012**, *134*, 17396.

[6] J. H. Heo, S. H. Im, J. H. Noh, T. N. Mandal, C.-S. Lim, J. A. Chang, Y. H. Lee, H.-j Kim, A. Sarkar, M. K. Nazeeruddin, M. Grätzel, S. I. Seok, *Nat. Photonics* **2013**, *7*, 486.

[7] NREL Best Research-Cell Efficiencies, www.nrel.gov/ncpv/images/efficiency_chart.jpg (accessed: March, **2015**).

[8] C. C. Stoumpos, C. D. Malliakas, M. G. Kanatzidis, *Inorg. Chem.* **2013**, *52*, 9019.

[9] M. M. Lee, J. Teuscher, T. Miyasaka, T. N. Murakami, H. Snaith, *Science* **2012**, *338*, 643.

[10] J. H. Noh, S. H. Im, J. H. Heo, T. N. Mandal, S. I. Seok, *Nano Lett.* **2013**, *13*, 1764.

[11] N. Pellet, P. Gao, G. Gregori, T.-Y. Yang, M. K. Nazeeruddin, J. Maier, M. Grätzel, *Angew. Chem. Int. Ed.* **2014**, *53*, 3151.

[12] N. K. Noel, S. D. Stranks, A. Abate, C. Wehrenfennig, S. Guarnera, A. A. Haghighirad, A. Sadhanala, G. E. Eperson, M. B. Johnston, A. M. Petrozza, L. M. Herz, H. J. Snaith, *Energy Environ. Sci.* **2014**, *7*, 3061.

[13] O. Malinkiewicz, A. Yella, Y. H. Lee, G. M. Espallargas, M. Grätzel, M. K. Nazeeruddin, H. J. Bolink, *Nat. Photonics* **2014**, *6*, 128.

[14] D. Liu, T. L. Kelly, *Nat. Photonics* **2014**, *8*, 133.

[15] Q. Chen, H. Zhou, Z. Hong, S. Luo, H.-S. Duan, H.-H. Wang, Y. Liu, G. Li, Y. Yang, *J. Am. Chem. Soc.* **2014**, *136*, 622.

[16] J. Burschka, N. Pellet, S.-J. Moon, R. Humphry-Baker, P. Gao, M. K. Nazeeruddin, M. Grätzel, *Nature* **2013**, *499*, 316.

[17] M. Liu, M. B. Johnston, H. J. Snaith, *Nature* **2013**, *501*, 395.

[18] M. Xiao, F. Huang, Y. Dkhissi, Y. Zhu, J. Etheridge, A. Gray-Weale, U. Bach, Y.-B. Cheng, L. Spiccia, *Angew. Chem. Int. Ed.* **2014**, *53*, 1.

[19] N. J. Jeon, J. H. Noh, Y. H. Kim, W. S. Yang, S. Ryu, S. I. Seok, *Nat. Mater.* **2014**, *13*, 897.

[20] G. E. Eperson, V. M. Burlakov, P. Docampo, A. Goriely, H. J. Snaith, *Adv. Funct. Mater.* **2014**, *24*, 151.

[21] G. E. Eperson, V. M. Burlakov, A. Goriely, H. J. Snaith, *ACS Nano* **2014**, *8*, 591.

[22] N. J. Jeon, J. H. Noh, W. S. Yang, Y. C. Kim, S. Ryu, J. Seo, S. I. Seok, *Nature* **2015**, *517*, 476.

[23] Y. Wu, A. Islam, X. Yang, C. Qin, J. Liu, K. Zhang, W. Peng, L. Han, *Energy Environ. Sci.* **2014**, *7*, 2934.

[24] Z. Xiao, Q. Dong, C. Bi, Y. Shao, Y. Yuan, J. Huang, *Adv. Mater.* **2014**, *26*, 6503.

[25] H. Zhou, Q. Chen, G. Li, S. Luo, T.-B. Song, H.-S. Duan, Z. Hong, J. You, Y. Liu, Y. Yang, *Science* **2014**, *345*, 542.

[26] Q. Chen, H. Zhou, T.-B. Song, S. Luo, Z. Hong, H.-S. Duan, L. Dou, Y. Liu, Y. Yang, *Nano Lett.* **2014**, *14*, 4158.

[27] L. Wang, C. McCleese, A. Kovalsky, Y. Zhao, C. Burda, *J. Am. Chem. Soc.* **2014**, *136*, 12205.

[28] M. Ikeda, M. Atsuta, A. Kinno, M. Tanaka, Y. Sugawara, (Toshiba) *US20010008271*, **2001**.